

**Microscopic analysis of shape evolution and triaxiality in germanium isotopes**

T. Nikšić, P. Marević, and D. Vretenar

*Physics Department, Faculty of Science, University of Zagreb, 10000 Zagreb, Croatia*

(Received 19 March 2014; published 29 April 2014)

**Background:** The motivation for this study is the experimental evidence for rigid triaxial deformation at low energy in  $^{76}\text{Ge}$  that was recently observed.

**Purpose:** Quadrupole shapes and low-energy spectra of the isotopes  $^{72-82}\text{Ge}$  are analyzed using a theoretical framework based on nuclear density functional theory.

**Method:** The relativistic functional DD-PC1, supplemented by a finite-range pairing force, is used to perform constrained triaxial mean-field calculations of energy surfaces as functions of quadrupole deformation parameters. The corresponding collective Hamiltonian, based on DD-PC1, is employed in the calculation of excitation spectra and transition rates.

**Results:** Model calculations reproduce the empirical trend of collective observables and predict the evolution of shapes from weakly triaxial in  $^{74}\text{Ge}$  to  $\gamma$  soft in  $^{78,80}\text{Ge}$ . For  $^{76}\text{Ge}$ , in particular, the theoretical excitation spectrum is in good agreement with available data, the experimental ratio  $E(2_2^+)/E(2_1^+)$  is reproduced, as well as the pattern and amplitude of the staggering in energy between odd- and even-spin states in the  $\gamma$  band.

**Conclusions:** The mean-field potential of  $^{76}\text{Ge}$  appears to be  $\gamma$  soft. Collective correlations drive the nucleus toward triaxiality but do not stabilize a rigid triaxial shape. Both the experimental and theoretical staggering of levels in the  $\gamma$  band display a pattern consistent with triaxial shapes but the amplitudes are negligible and do not present evidence for rigid triaxiality.

DOI: [10.1103/PhysRevC.89.044325](https://doi.org/10.1103/PhysRevC.89.044325)

PACS number(s): 21.60.Jz, 21.60.Ev, 21.10.Re

**I. INTRODUCTION**

The great majority of nonspherical atomic nuclei display axially symmetric quadrupole deformed shapes; that is, their equilibrium shapes correspond to prolate or oblate ellipsoids. In a number of nuclei, however, axial symmetry is explicitly broken and the corresponding ellipsoid can be characterized by a certain degree of triaxiality. And while empirical evidence of stable triaxial shapes has been established in the excitation region of relatively high angular momenta [1–5], static triaxiality in equilibrium nuclear configurations still presents an open question, both experimentally and in microscopic nuclear structure theories. Static quadrupole shape deformations can be described in terms of the polar deformation parameters  $\beta$  and  $\gamma$  [6]. The parameter  $\beta$  is proportional to the intrinsic quadrupole moment, and the angular variable  $\gamma$  specifies the shape. The limit  $\gamma = 0$  corresponds to axial prolate shapes, whereas the shape is oblate for  $\gamma = \pi/3$ . Intermediate values  $0 < \gamma < \pi/3$  are associated with triaxial shapes. Most theoretical analyses of triaxiality have been based on two simple elementary models: (i) the rigid-triaxial rotor model of Davydov and Filippov (DF) [7], and (ii) the  $\gamma$ -unstable rotor model of Wilets and Jean (WJ) [8]. The assumption of the DF model is that the collective potential has a stable minimum at a particular value of  $\gamma$  ( $\gamma$ -rigid potential), whereas in the WJ model the potential is independent of  $\gamma$  and thus the corresponding collective wave functions are extended in the  $\gamma$  direction ( $\gamma$ -soft potential).

The type of  $\gamma$  deformation and the degree of triaxiality is difficult to identify from low-spin data because both the DF and the WJ models predict similar excitation energies and  $B(E2)$  values for transitions within the ground-state band. Fortunately,  $\gamma$  bands are much more sensitive to triaxial

deformation and, in particular, the pattern of odd- and even-spin level staggering in the  $\gamma$  band is different for  $\gamma$ -rigid and  $\gamma$ -soft triaxial shapes [9,10]. In a recent microscopic study [11] based on nuclear density functional theory (DFT), we investigated the emergence of  $\gamma$  deformation for a large set of representative nonaxial medium-heavy and heavy nuclei. Starting from microscopic energy surfaces as functions of the polar deformation parameters  $\beta$  and  $\gamma$ , we calculated and analyzed the systematics of low-lying collective spectra and transition rates. The analysis has clearly demonstrated that neither the limit of rigid-triaxial rotor (DF) nor the  $\gamma$  unstable rotor limit (WJ) are actually realized in nuclei. As a robust regularity in the low-spin excitation spectra, we found that typical nonaxial medium-heavy and heavy nuclei lie almost exactly in the middle between the two geometrical limits.

Experimental evidence for rigid triaxial deformation at low energy in  $^{76}\text{Ge}$  has recently been reported in Ref. [12]. The  $\gamma$  band of this nucleus was extended and analyzed up to spin  $9^+$ . It was shown that the phase of the odd-even staggering of the  $\gamma$  band is consistent with the assumption of a  $\gamma$ -rigid structure, although the amplitude of the staggering is considerably smaller than that predicted by the DF model. More specifically, the  $E(2_2^+)/E(2_1^+)$  ratio, the phase of a staggering parameter that quantifies how adjacent levels within the  $\gamma$  band are grouped, and the  $B(E2)$  ratios are reproduced by the DF model, thus suggesting a shape with near maximum triaxiality  $\gamma \approx 30^\circ$ . The problem, however, is that the amplitude of the observed staggering is significantly smaller than the DF model prediction for  $\gamma = 30^\circ$ . The calculated staggering amplitude can be reduced by decreasing  $\gamma$  but this increases the excitation energy of the  $\gamma$  band significantly, in disagreement with experiment. In Ref. [12] the  $\gamma$ -band data were also compared to results of a phenomenological pairing-plus-quadrupole

shell-model calculation [13]. It was noted that, using single-particle energies adjusted to reproduce the energy spectra of low-lying states in neighboring odd- $A$  nuclei, and adjusting the interaction strengths to fit the energy levels of yrast and other low-lying states of odd- $A$  and even-even nuclei in this mass region [13], shell-model calculations reproduce both the phase and the magnitude of the  $\gamma$ -band staggering in  $^{76}\text{Ge}$ .

The evolution of triaxiality in Ge and Se nuclei and, in particular, the rigid  $\gamma$  deformation at low-spin in  $^{76}\text{Ge}$ , has very recently been investigated in the framework of the multiquasiparticle triaxial projected shell model (TPSM) [14]. It has been shown that to reproduce the data for both the yrast and  $\gamma$ -vibrational bands of  $^{76}\text{Ge}$ , a fixed triaxial deformation parameter  $\gamma \approx 30^\circ$  is required for the TPSM calculation, consistent with the prediction of the DF model. In a systematic study of neighboring nuclei it has also been demonstrated that configuration mixing of various quasiparticle states can result in a dynamical change from a  $\gamma$ -rigid structure to  $\gamma$ -soft shapes.

The purpose of the present work is to analyze the shapes and low-energy spectra of the isotopes  $^{72-82}\text{Ge}$  using a theoretical framework based on nuclear density functional theory. Nuclear energy density functionals (EDFs) provide an accurate description of equilibrium mean-field properties and collective excitations over the entire chart of nuclides. When compared to the shell-model approach, already at the self-consistent mean-field (SCMF) level one of the principal advantages is the use of global effective interactions that can be applied to all mass regions. Another strong point are model spaces that include all occupied states (no distinction between core and valence nucleons, no need for effective charges) and, of course, mean-field results can be interpreted using intuitive picture of intrinsic shapes. To compute excitation spectra and transition rates, however, the EDF framework has to be extended to take into account the restoration of symmetries broken in the mean-field approximation, and fluctuations in the collective coordinates. The quadrupole collective model Hamiltonian that will be used in this study is based on constrained triaxial self-consistent mean-field calculations, including  $\beta$  and  $\gamma$  deformations. The resulting self-consistent solutions (single-nucleon wave functions, occupation probabilities and quasiparticle energies) that correspond to individual points on the constrained energy surface are used to calculate the parameters of the collective Hamiltonian: three mass parameters, three moments of inertia, and the zero-point energy correction [15]. The subsequent diagonalization of the Hamiltonian yields the excitation energies and collective wave functions that are used to calculate observables. In the present calculation the relativistic functional DD-PC1 [16] is used in the particle-hole channel, and a finite-range pairing force separable in momentum space in the particle-particle channel [17]. The semimicroscopic relativistic functional DD-PC1 was adjusted to the experimental masses of a set of 64 deformed nuclei in the mass regions  $A \approx 150-180$  and  $A \approx 230-250$ , and further tested in a number of mean-field and beyond-mean-field calculations in different mass regions [18]. The pairing interaction is completely determined by two parameters adjusted to reproduce the empirical bell-shaped pairing gap in symmetric nuclear matter [19].

We note that, on the self-consistent mean-field level, the ground-state deformations of the Ge isotopes were also investigated in the framework of Gogny–Hartree–Fock–Bogoliubov (HFB) theory, and the Skyrme Hartree–Fock plus pairing in the BCS approximation [20]. Five different Skyrme parametrizations were used to explore the influence of different effective masses and spin-orbit models. All the models predict the occurrence of triaxial shapes in Ge isotopes, with only few exceptions that can be attributed to neutron subshell closures. The general softness of the Ge isotopes with respect to nonaxial deformations was nicely illustrated by computing constrained triaxial potential energy surfaces.

## II. EVOLUTION OF SHAPES IN $^{72-82}\text{Ge}$

Our microscopic analysis of shape evolution in the chain of  $^{72-82}\text{Ge}$  isotopes starts with a self-consistent relativistic Hartree–Bogoliubov (RHB) [21,22] calculation of quadrupole binding energy surfaces. The Dirac–Hartree–Bogoliubov equations are solved by expanding the nucleon spinors in the basis of a three-dimensional (3D) harmonic oscillator in Cartesian coordinates. The map of the energy surface as a function of quadrupole deformation is obtained by imposing constraints on the axial and triaxial mass quadrupole moments. The method of quadratic constraint [23] uses an unrestricted variation of the function

$$\langle \hat{H} \rangle + \sum_{\mu=0,2} C_{2\mu} (\langle \hat{Q}_{2\mu} \rangle - q_{2\mu})^2, \quad (1)$$

where  $\langle \hat{H} \rangle$  is the total energy, and  $\langle \hat{Q}_{2\mu} \rangle$  denotes the expectation value of the mass quadrupole operators,

$$\hat{Q}_{20} = 2z^2 - x^2 - y^2 \quad \text{and} \quad \hat{Q}_{22} = x^2 - y^2, \quad (2)$$

$q_{2\mu}$  is the constrained value of the multipole moment, and  $C_{2\mu}$  is the corresponding stiffness constant.

In Fig. 1 we display the RHB triaxial quadrupole energy maps of the even-even isotopes  $^{72-82}\text{Ge}$  in the  $\beta$ - $\gamma$  plane ( $0 \leq \gamma \leq 60^\circ$ ). For each nucleus energies are normalized with respect to the binding energy of the absolute minimum. Because of the  $N = 40$  subshell closure  $^{72}\text{Ge}$  displays a pronounced spherical minimum. By adding just two more neutrons a pronounced triaxial minimum at  $(\beta, \gamma) = (0.25, 32^\circ)$  develops in  $^{74}\text{Ge}$ . Additional neutrons at first lead to a softening of the energy surface in the  $\gamma$  direction, resulting in the axially symmetric minimum on the prolate axis for the isotopes  $^{76-80}\text{Ge}$ . Finally,  $^{82}\text{Ge}$  is a semispherical nucleus.

The variation of mean-field shapes in an isotopic chain is governed by the evolution of the underlying shell structure of single-nucleon orbitals. The formation of deformed minima is related to the occurrence of regions of low single-particle level density around the Fermi surface. In Figs. 2–4 we plot the proton and neutron single-particle energy levels in the canonical basis for the nuclei  $^{74,76,78}\text{Ge}$ . Solid (blue) and dashed (red) curves correspond to levels with positive and negative parity, respectively. The dot-dashed (green) curves denote the Fermi level. The single-particle levels are plotted as functions of the deformation parameters along closed paths in the  $\beta$ - $\gamma$  plane. The panels on the left and right display prolate ( $\gamma = 0^\circ$ ) and oblate ( $\gamma = 60^\circ$ ) axially symmetric

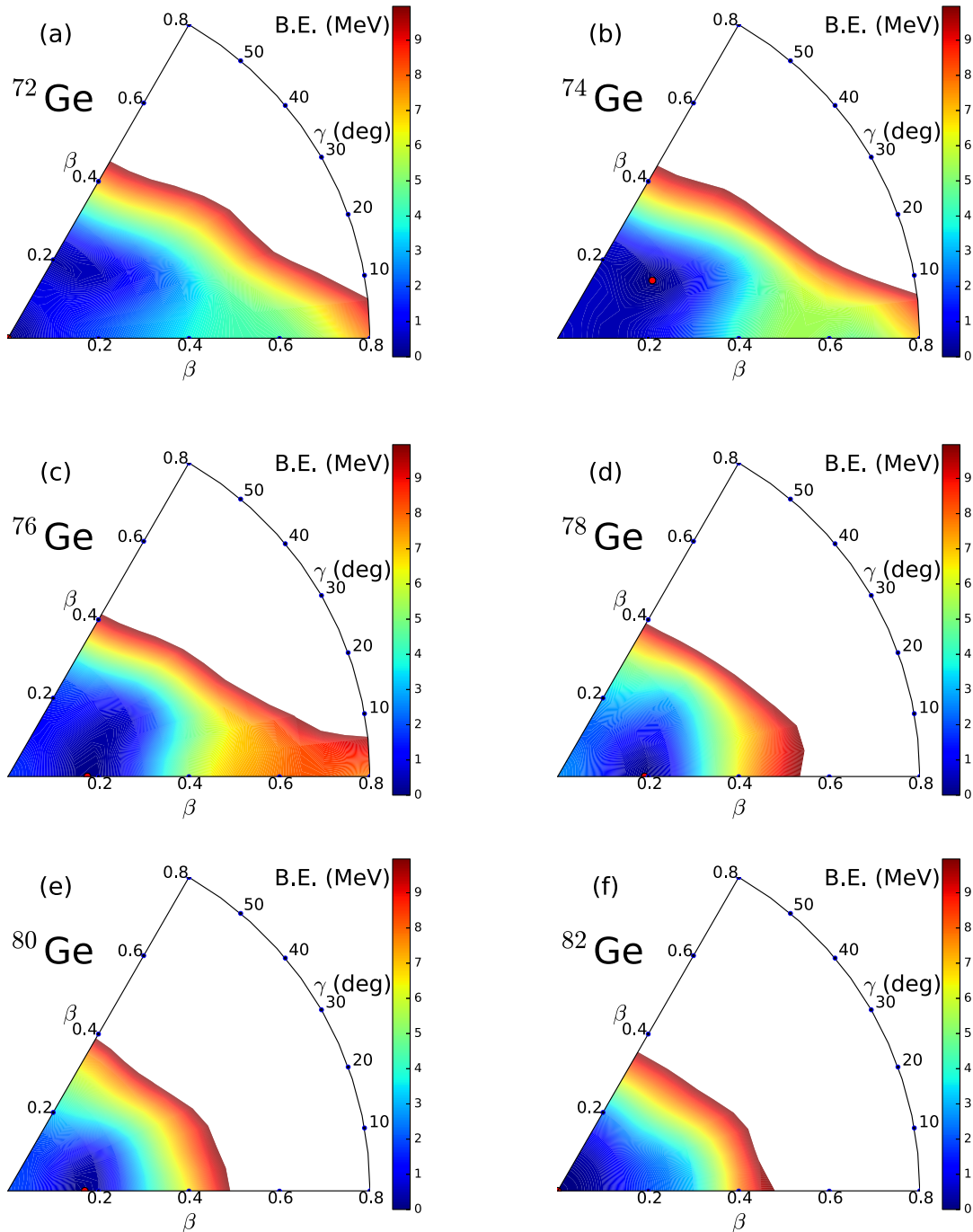


FIG. 1. (Color online) Self-consistent RHB triaxial energy surfaces of even-even Ge nuclei in the  $\beta$ - $\gamma$  plane ( $0 \leq \gamma \leq 60^\circ$ ). For each nucleus energies are normalized with respect to the binding energy of the absolute minimum.

single-particle levels, respectively. In the middle panel of each figure the proton and neutron levels are plotted as functions of  $\gamma$ , for a fixed value of the axial deformation  $|\beta|$  at the position of equilibrium minimum of the binding energy surface. This means that, starting from the spherical configuration, one follows the single-nucleon levels on a path along the prolate axis up to the approximate position of the minimum (left panel). Next, for this fixed value of  $|\beta|$  we trace the levels along the path from  $\gamma = 0^\circ$  to  $\gamma = 60^\circ$  (middle panel) and, finally, back to the spherical configuration along the oblate

axis (right panel). Configurations along the oblate axis are denoted by negative values of  $\beta$ . For  $^{74}\text{Ge}$  one notices that the proton levels display a pronounced gap between the last occupied and first unoccupied levels in the triaxial region at  $\gamma \approx 30^\circ$ . For the neutron levels the gap appears to be almost independent of  $\gamma$ . Combined self-consistently, the proton and neutron gaps lead to the formation of the triaxial minimum on the energy surface shown in Fig. 1. This microscopic picture does not change for the proton levels of  $^{76}\text{Ge}$  (Fig. 3) and  $^{78}\text{Ge}$  (Fig. 4), but the neutron levels display a tendency towards

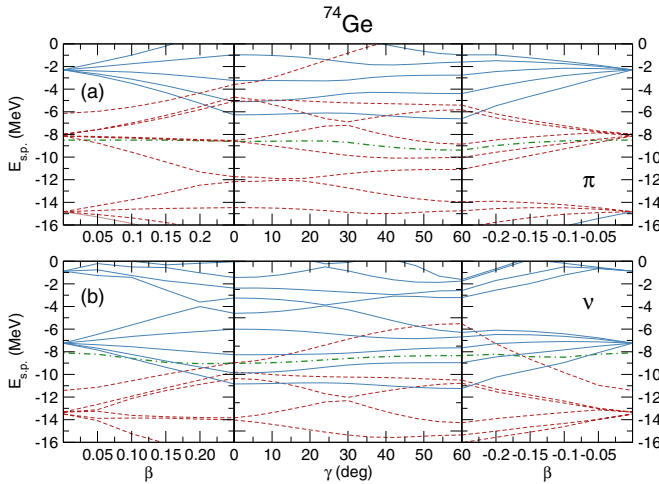


FIG. 2. (Color online) Single-proton and single-neutron energy levels of  $^{74}\text{Ge}$  as functions of the deformation parameters along closed paths in the  $\beta$ - $\gamma$  plane. Solid (blue) and dashed (red) curves correspond to levels with positive and negative parity, respectively. The dot-dashed (green) curves denote the Fermi level. The panels on the left and right display prolate ( $\gamma = 0^\circ$ ) and oblate ( $\gamma = 60^\circ$ ) axially symmetric single-nucleon levels, respectively. In the middle panel of each figure the proton and neutron levels are plotted as functions of  $\gamma$  for a fixed value of the axial deformation  $|\beta|$  that corresponds to the mean-field minimum.

prolate axially symmetric deformation. The dependence of the energy on the triaxial deformation parameter  $\gamma$  is illustrated even more clearly with the projections shown in Fig. 5, where we plot the self-consistent RHB constrained energy curves of  $^{74}\text{Ge}$ ,  $^{76}\text{Ge}$ , and  $^{78}\text{Ge}$  as functions of  $\gamma$ , at fixed values of the axial deformation:  $\beta = 0.25$ ,  $\beta = 0.20$ , and  $\beta = 0.20$ , respectively, that correspond to the positions of the mean-field minima in Fig. 1. One notices that  $^{74}\text{Ge}$  displays a shallow triaxial minimum at  $\gamma = 30^\circ$ , whereas the isotopes  $^{76}\text{Ge}$  and  $^{78}\text{Ge}$  have axially symmetric minima. The magnitude of the  $\gamma$  dependence of the energy is similar for  $^{74}\text{Ge}$  and  $^{76}\text{Ge}$ ,

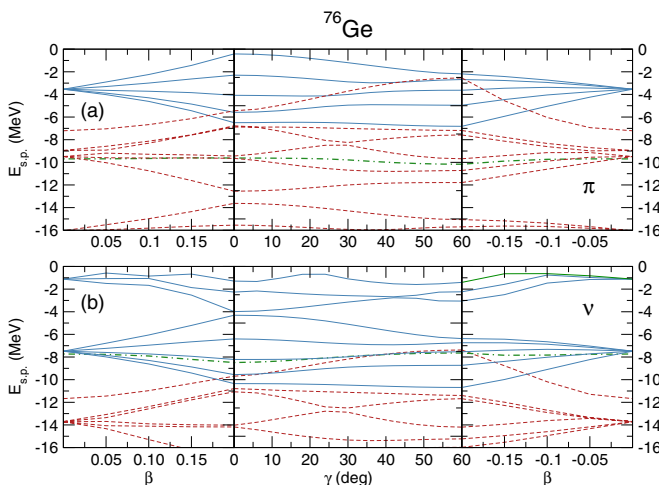


FIG. 3. (Color online) Same as described in the caption to Fig. 2 but for the nucleus  $^{76}\text{Ge}$ .

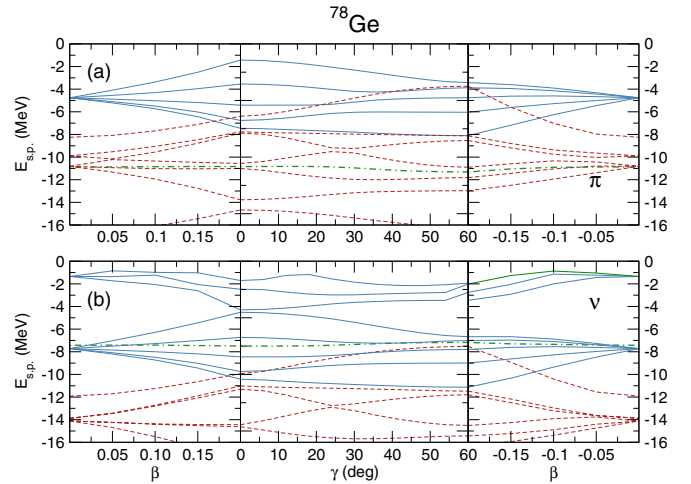


FIG. 4. (Color online) Same as described in the caption to Fig. 2 but for the nucleus  $^{78}\text{Ge}$ .

whereas it is considerably stiffer for  $^{78}\text{Ge}$ . In all three cases, however, the difference in energy between the prolate and triaxial configurations is less than 1.5 MeV and, in particular, for  $^{76}\text{Ge}$  the prolate minimum is located only 0.5 MeV below the triaxial  $\gamma = 30^\circ$  configuration. Such a small energy difference between mean-field configurations characterized by different deformation parameters indicate a potentially decisive role of dynamical effects related to restoration of broken symmetries and fluctuations in collective coordinates. As shown in the global study of quadrupole correlation effects of Ref. [24], typically nuclei below mass  $A \leq 60$  display larger dynamical correlation energy than static deformation energy (energy difference between the spherical configuration and the deformed equilibrium configuration), whereas heavier deformed nuclei have larger static deformation energy than collective correlation energy.

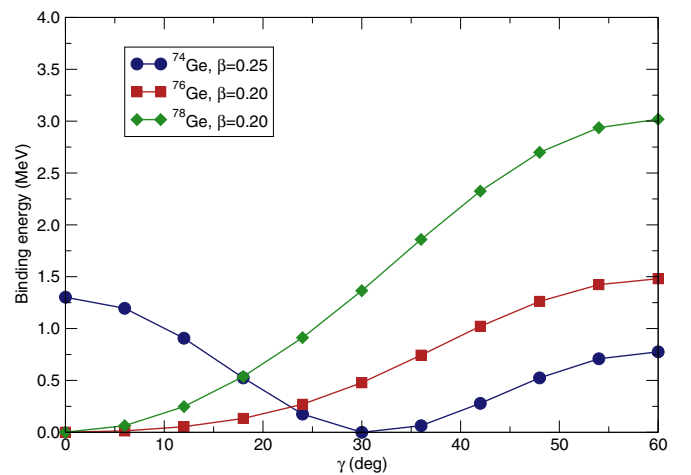


FIG. 5. (Color online) Self-consistent RHB constrained energy curves of  $^{74}\text{Ge}$ ,  $^{76}\text{Ge}$ , and  $^{78}\text{Ge}$  as functions of the deformation parameter  $\gamma$ , at fixed values of the axial deformation:  $\beta = 0.25$ ,  $\beta = 0.20$ , and  $\beta = 0.20$ , respectively. For each nucleus energies are normalized with respect to the binding energy of the absolute minimum.

To include collective correlations and, therefore, to enable calculation of excitation spectra and transition rates, a collective Hamiltonian can be formulated that restores rotational symmetry and accounts for fluctuations around the axial or triaxial mean-field minima. The dynamics of the five-dimensional Hamiltonian for quadrupole vibrational and rotational degrees of freedom is governed by the seven functions of the intrinsic deformations  $\beta$  and  $\gamma$ : the collective potential, the three vibrational mass parameters:  $B_{\beta\beta}$ ,  $B_{\beta\gamma}$ ,  $B_{\gamma\gamma}$ , and three moments of inertia for rotations around the principal axes. The microscopic self-consistent solutions of the constrained triaxial RHB equations, i.e., the single-quasiparticle energies

and wave functions for the entire energy surface as functions of the quadrupole deformations, provide the microscopic input for the parameters of the collective Hamiltonian [15]. The five quadrupole collective coordinates are parameterized in terms of two deformation parameters  $\beta$  and  $\gamma$  and three Euler angles  $(\phi, \theta, \psi) \equiv \Omega$ , which define the orientation of the intrinsic principal axes in the laboratory frame. The collective Hamiltonian reads

$$\hat{H} = \hat{T}_{\text{vib}} + \hat{T}_{\text{rot}} + V_{\text{coll}}, \quad (3)$$

with the vibrational kinetic energy

$$\begin{aligned} \hat{T}_{\text{vib}} = & -\frac{\hbar^2}{2\sqrt{wr}} \left\{ \frac{1}{\beta^4} \left[ \frac{\partial}{\partial\beta} \sqrt{\frac{r}{w}} \beta^4 B_{\gamma\gamma} \frac{\partial}{\partial\beta} - \frac{\partial}{\partial\beta} \sqrt{\frac{r}{w}} \beta^3 B_{\beta\gamma} \frac{\partial}{\partial\gamma} \right] \right. \\ & \left. + \frac{1}{\beta \sin 3\gamma} \left[ -\frac{\partial}{\partial\gamma} \sqrt{\frac{r}{w}} \sin 3\gamma B_{\beta\gamma} \frac{\partial}{\partial\beta} + \frac{1}{\beta} \frac{\partial}{\partial\gamma} \sqrt{\frac{r}{w}} \sin 3\gamma B_{\beta\beta} \frac{\partial}{\partial\gamma} \right] \right\}, \end{aligned} \quad (4)$$

and rotational kinetic energy

$$\hat{T}_{\text{rot}} = \frac{1}{2} \sum_{k=1}^3 \frac{\hat{J}_k^2}{\mathcal{I}_k}. \quad (5)$$

$V_{\text{coll}}$  is the collective potential.  $\hat{J}_k$  denotes the components of the angular momentum in the body-fixed frame of a nucleus, and the mass parameters  $B_{\beta\beta}$ ,  $B_{\beta\gamma}$ ,  $B_{\gamma\gamma}$ , as well as the moments of inertia  $\mathcal{I}_k$ , depend on the quadrupole deformation variables  $\beta$  and  $\gamma$ :

$$\mathcal{I}_k = 4B_k\beta^2 \sin^2(\gamma - 2k\pi/3). \quad (6)$$

Two additional quantities that appear in the expression for the vibrational energy:  $r = B_1 B_2 B_3$ , and  $w = B_{\beta\beta} B_{\gamma\gamma} - B_{\beta\gamma}^2$ , determine the volume element in the collective space.

The collective potential, the mass parameters, and the moments of inertia are determined by the microscopic nuclear energy density functional and the effective interaction in the  $pp$  channel. In the current implementation of the model the moments of inertia are computed using the Inglis–Belyaev formula:

$$\mathcal{I}_k = \sum_{i,j} \frac{|\langle ij | \hat{J}_k | \Phi \rangle|^2}{E_i + E_j}, \quad k = 1, 2, 3, \quad (7)$$

where  $k$  denotes the axis of rotation, the summation runs over proton and neutron quasiparticle states  $|ij\rangle = \beta_i^\dagger \beta_j^\dagger |\Phi\rangle$ , and  $|\Phi\rangle$  represents the quasiparticle vacuum. The mass parameters associated with the two quadrupole collective coordinates  $q_0 = \langle \hat{Q}_{20} \rangle$  and  $q_2 = \langle \hat{Q}_{22} \rangle$  are calculated in the cranking approximation:

$$B_{\mu\nu}(q_0, q_2) = \frac{\hbar^2}{2} [\mathcal{M}_{(1)}^{-1} \mathcal{M}_{(3)} \mathcal{M}_{(1)}^{-1}]_{\mu\nu}, \quad (8)$$

where

$$\mathcal{M}_{(n),\mu\nu}(q_0, q_2) = \sum_{i,j} \frac{|\langle \Phi | \hat{Q}_{2\mu} | ij \rangle \langle ij | \hat{Q}_{2\nu} | \Phi \rangle|}{(E_i + E_j)^n}. \quad (9)$$

Finally, the potential  $V_{\text{coll}}$  in the collective Hamiltonian (3) is obtained by subtracting the zero-point energy corrections from the total energy that corresponds to the solution of constrained RHB equations, at each point on the triaxial deformation plane [15].

The Hamiltonian of Eq. (3) describes quadrupole vibrations, rotations, and the coupling of these collective modes. The diagonalization yields the excitation energies and collective wave functions:

$$\Psi_\alpha^{JM}(\beta, \gamma, \Omega) = \sum_{K \in \Delta J} \psi_{\alpha K}^J(\beta, \gamma) \Phi_{MK}^J(\Omega). \quad (10)$$

The angular part corresponds to linear combinations of Wigner functions

$$\Phi_{MK}^J(\Omega) = \sqrt{\frac{2J+1}{16\pi^2(1+\delta_{K0})}} [D_{MK}^{J*}(\Omega) + (-1)^J D_{M-K}^{J*}(\Omega)], \quad (11)$$

and the summation in Eq. (10) is over the allowed set of the  $K$  values:

$$\Delta J = \begin{cases} 0, 2, \dots, J & \text{for } J \bmod 2 = 0 \\ 2, 4, \dots, J-1 & \text{for } J \bmod 2 = 1. \end{cases} \quad (12)$$

By using the collective wave functions of Eq. (10), various observables can be calculated and compared to experimental results. For instance, the quadrupole  $E2$  reduced transition probability:

$$B(E2; \alpha J \rightarrow \alpha' J') = \frac{1}{2J+1} |\langle \alpha' J' | \hat{\mathcal{M}}(E2) | \alpha J \rangle|^2, \quad (13)$$

where  $\hat{\mathcal{M}}(E2)$  is the electric quadrupole operator.

The quality with which model calculations reproduce the trend of available data is illustrated in Fig. 6 where we plot the isotopic dependence of two characteristic collective observables: the ratio  $R_{4/2}$  between the excitation energies of the first  $4^+$  and  $2^+$  states, and the  $B(E2; 2_1^+ \rightarrow 0_1^+)$  values in Weisskopf units. The theoretical values obtained by the

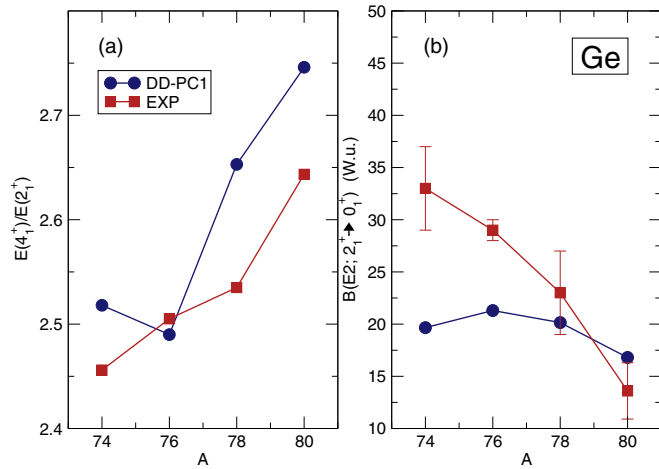


FIG. 6. (Color online) Evolution of the ratio between the excitation energies of the first  $4^+$  and  $2^+$  states (left panel), and the  $B(E2; 2_1^+ \rightarrow 0_1^+)$  values in Weisskopf units (right panel), with mass number for the Ge isotopes.

diagonalization of the collective Hamiltonian, with parameters determined by the relativistic energy density functional DD-PC1 and the separable pairing force, are shown in comparison with data [25]. The model reproduces the empirical trend of increase of  $R_{4/2}$  with neutron number and, in particular, the experimental value for  $^{76}\text{Ge}$ . The calculated  $B(E2)$  values are in good overall agreement with data, even although the rapid decrease of experimental values with neutron number is not reproduced by the model. It appears that the collective wave functions of the yrast states show little variations with mass number for  $A \leq 80$ .

To analyze in more detail the level of quantitative agreement between our microscopic model calculation and data, in Fig. 7 we plot the excitation spectrum of  $^{76}\text{Ge}$  calculated with the collective Hamiltonian. Levels that belong to the ground-state band and the  $\gamma$  band are shown in comparison to the exper-

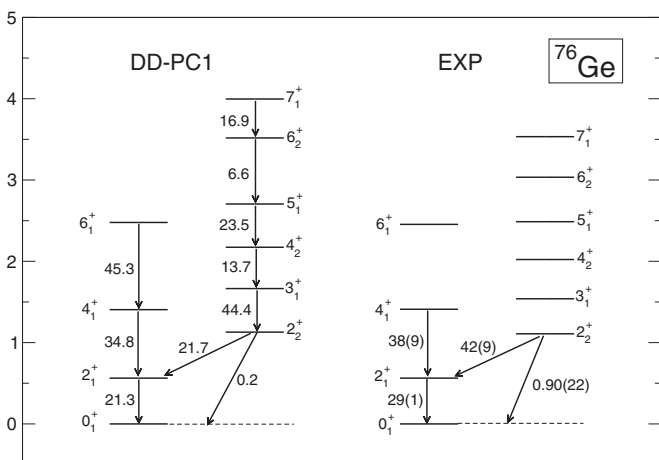


FIG. 7. The excitation spectrum of  $^{76}\text{Ge}$  calculated with the collective Hamiltonian based on the DD-PC1 relativistic density functional (left) compared to data [12,25] (right). The  $B(E2)$  values are given in Weisskopf units.

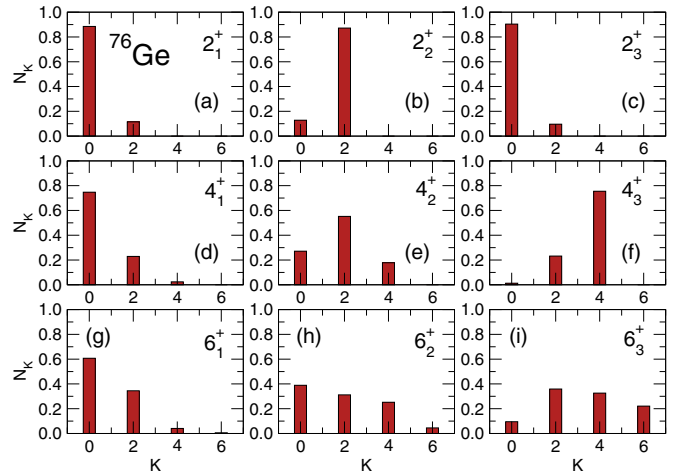


FIG. 8. (Color online) Distribution of  $K$  components (projection of the angular momentum on the body-fixed symmetry axis) in the collective wave functions of the nucleus  $^{76}\text{Ge}$ .

imental spectrum [12,25]. The theoretical levels are assigned either to the ground-state band or the  $\gamma$  band according to the distribution of the projection  $K$  of the angular momentum  $J$  on the  $z$  axis in the body-fixed frame. Yrast states have a predominant  $K = 0$  component in the wave functions, whereas the  $\gamma$  band comprises states above the yrast characterized by dominant  $K = 2$  components. The calculated excitation energies have been rescaled to reproduce the experimental energy of the state  $2_1^+$ . This scaling is necessary because of the well-known fact that the Inglis–Belyaev (IB) moments of inertia and cranking mass parameters are actually smaller than the corresponding empirical values, due to the omission of time-odd components of the mean-field (the so-called Thouless–Valatin dynamical rearrangement contributions). Of course, the *a posteriori* scaling does not affect the collective wave functions and transition rates. One notices that the calculation reproduces the experimental spectrum, both the excitation energies as well as the available  $B(E2)$  values. In particular, the band head  $2_\gamma$  is predicted at the excitation energy of the level  $2_2^+$ , but the theoretical  $\gamma$  band is somewhat spread out compared to the experimental sequence and the calculated  $B(E2)$  values for transitions within this band point to considerable  $K$  mixing for states with higher angular momenta. This is explicitly shown in Fig. 8 where we display the distribution of  $K$  components in the collective wave functions of the lowest states with angular momenta  $2^+$ ,  $4^+$ , and  $6^+$ :

$$N_K = 6 \int_0^{\pi/3} \int_0^\infty |\psi_{\alpha,K}^J(\beta, \gamma)|^2 \beta^4 |\sin 3\gamma| d\beta d\gamma. \quad (14)$$

The  $\psi_{\alpha,K}^J(\beta, \gamma)$  components are defined in Eq. (10). A broader distribution of  $N_K$  values in the state  $|\alpha J\rangle$  provides a measure of mixing of intrinsic configurations.

The level of  $K$  mixing is reflected in the staggering in energy between odd- and even-spin states in the  $\gamma$  band. The staggering can be quantified by considering the following

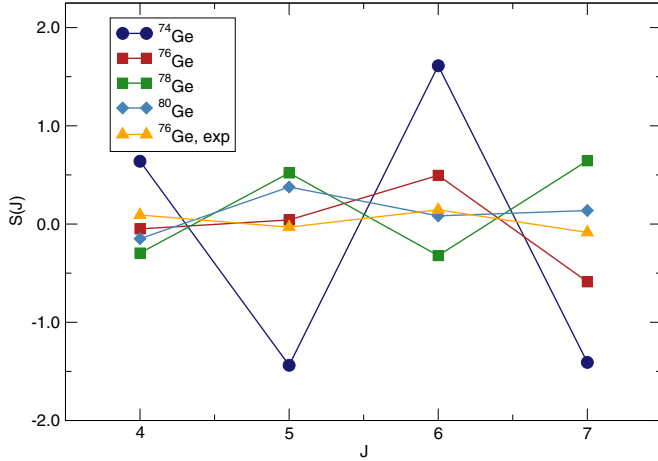


FIG. 9. (Color online) Staggering  $S(J)$  [Eq. (15)] in the  $\gamma$  bands of  $^{74-80}\text{Ge}$  isotopes.

differential quantity [9]:

$$S(J) = \frac{E[J_\gamma^+] - 2E[(J-1)_\gamma^+] + E[(J-2)_\gamma^+]}{E[2_1^+]}. \quad (15)$$

$S(J)$  measures the displacement of the  $(J-1)_\gamma^+$  level relative to the average of its neighbors  $J_\gamma^+$  and  $(J-2)_\gamma^+$ , normalized to the energy of the first-excited state of the ground-state band  $2_1^+$ . The differential form of the  $S(J)$  makes it extremely sensitive to the shape of a nucleus. For an axially symmetric rotor  $S(J)$  is constant. In a study of staggering of  $\gamma$ -band energies and the transition between different structural symmetries in nuclei [10], the experimental energy staggering in  $\gamma$  bands of several isotopic chains was investigated as a signature for the  $\gamma$  dependence of the potential. For a nucleus with a deformed  $\gamma$ -soft potential,  $S(J)$  oscillates between negative values for even-spin states and positive values for odd-spin states, with the magnitude slowly increasing with spin. For a triaxial potential the level clustering in the  $\gamma$  band is opposite, and  $S(J)$  oscillates between positive values for even-spin states and negative values for odd-spin states. In this case the magnitude of  $S(J)$  increases more rapidly with spin, as compared to the  $\gamma$ -soft potential.

Figure 9 displays the calculated values for the staggering  $S(J)$  in the  $\gamma$  bands of the nuclei  $^{74-80}\text{Ge}$ . The experimental values for the isotope  $^{76}\text{Ge}$  [12] are also included in the figure. The results clearly show that the phase of the theoretical  $S(J)$  for  $^{74}\text{Ge}$  is consistent with the DF picture of a  $\gamma$ -rigid triaxial shape, although the amplitude of the staggering is considerably smaller than the one predicted by the DF model. On the other hand,  $^{78}\text{Ge}$  and  $^{80}\text{Ge}$  display the opposite pattern for  $S(J)$ ; that is, their  $\gamma$  bands indicate soft shapes.  $^{76}\text{Ge}$  appears to be at the transition point between the triaxial  $^{74}\text{Ge}$  and the  $\gamma$ -soft heavier isotopes. For this isotope the amplitudes of  $S(4)$  and  $S(5)$  almost vanish, whereas  $S(6)$  and  $S(7)$  follow a pattern characteristic for triaxial shapes, but with considerably smaller amplitudes. This cannot be considered as a robust indication of rigid triaxiality. As already emphasized in the introduction, in Ref. [12] it was noted that an amplitude much smaller than that predicted by the DF model could be explained by assuming

that the triaxial potential has a minimum at  $\gamma < 30^\circ$ , but this pushes the  $\gamma$  band higher in excitation energy, in contrast to the experimental ratio  $E(2_2^+)/E(2_1^+) = 2$ .

The present calculation reproduces the experimental ratio  $E(2_2^+)/E(2_1^+) = 2$ , the phase and the amplitude of the staggering  $S(J)$  for the low-spin levels of the  $\gamma$  band of  $^{76}\text{Ge}$ . States with higher angular momenta display such a pronounced level of fragmentation of different  $K$  components that it becomes impossible to identify members of the  $\gamma$  band ( $K = 2$ ) unequivocally. We emphasize that, in contrast to previous shell-model calculations [13,14] that provided support for rigid triaxial deformation at low energy in  $^{76}\text{Ge}$  but used single-particle energies and two-body interactions specifically tailored to spectroscopic data in this mass region, the present results have been obtained using a universal energy density functional (DD-PC1) and a pairing interaction that were not adjusted to the considered nuclei in any way. In fact, as already noted in the introduction, the parameters of the functional DD-PC1 were determined only by the empirical masses in the regions  $A \approx 150-180$  and  $A \approx 230-250$ . It is therefore remarkable that, without any further adjustment, the quadrupole collective Hamiltonian based on this functional yields results that are in such good agreement with available data for  $^{76}\text{Ge}$ .

### III. CONCLUSION

The framework of nuclear density functional theory has been used to analyze the evolution of quadrupole shapes in the isotopes  $^{72-82}\text{Ge}$ . The motivation for this study is the experimental evidence for rigid triaxial deformation at low energy in  $^{76}\text{Ge}$  that was recently reported in Ref. [12]. Employing the universal relativistic functional DD-PC1 [16], and a finite-range pairing force separable in momentum space [17], we have used the relativistic Hartree–Bogoliubov model to calculate the constrained energy surfaces of germanium isotopes as functions of the quadrupole deformation parameters  $\beta$  and  $\gamma$ . The resulting single-quasiparticle energies and wave functions for the entire energy surface as functions of the quadrupole deformations determine the parameters of the collective Hamiltonian [15] that are used to compute low-energy excitation spectra and electromagnetic transition rates.

The results for the energy surfaces (Figs. 1 and 5), for the spectrum of  $^{76}\text{Ge}$  (Fig. 7), and the staggering  $S(J)$  shown in Fig. 9, illustrate the evolution of shapes from weakly triaxial in  $^{74}\text{Ge}$  to  $\gamma$  soft in  $^{78,80}\text{Ge}$  and, finally, spherical in  $^{82}\text{Ge}$ . Even though our results are in very good agreement with available data for  $^{76}\text{Ge}$ , both for the ratio  $E(2_2^+)/E(2_1^+) = 2$  and the pattern and amplitude of the staggering  $S(J)$ , they do not confirm the evidence for rigid triaxial deformation at low energy in this nucleus. In fact, the present analysis indicates that the mean-field potential of  $^{76}\text{Ge}$  is  $\gamma$  soft. The inclusion of collective correlations (symmetry restoration and quantum fluctuations) drives the nucleus toward triaxiality, but they are not strong enough to stabilize a  $\gamma \approx 30^\circ$  triaxial shape. This is clearly reflected in both the experimental and calculated staggering  $S(J)$  which display a pattern consistent with triaxial shapes but the amplitudes are negligible and cannot be considered as evidence for rigid triaxiality.

- [1] S. W. Ødegård *et al.*, *Phys. Rev. Lett.* **86**, 5866 (2001).
- [2] G. Schönwaßer *et al.*, *Phys. Lett. B* **552**, 9 (2003).
- [3] D. J. Hartley *et al.*, *Phys. Rev. C* **80**, 041304(R) (2009).
- [4] T. Koike, K. Starosta, P. Joshi, G. Rainovski, J. Timár, C. Vaman, and R. Wadsworth, *J. Phys. G* **31**, S1741 (2005).
- [5] J. Meng and S. Q. Zhang, *J. Phys. G* **37**, 064025 (2010).
- [6] A. Bohr and B. R. Mottelson, *Nuclear Structure* (Benjamin, New York, 1969), Vol. I; *Nuclear Structure* (Benjamin, New York, 1975), Vol. II.
- [7] A. S. Davydov and G. F. Filipov, *Nucl. Phys.* **8**, 237 (1958).
- [8] L. Wilets and M. Jean, *Phys. Rev.* **102**, 788 (1956).
- [9] N. Zamfir and R. Casten, *Phys. Lett. B* **260**, 265 (1991).
- [10] E. A. McCutchan, D. Bonatsos, N. V. Zamfir, and R. F. Casten, *Phys. Rev. C* **76**, 024306 (2007).
- [11] K. Nomura, N. Shimizu, D. Vretenar, T. Nikšić, and T. Otsuka, *Phys. Rev. Lett.* **108**, 132501 (2012).
- [12] Y. Toh *et al.*, *Phys. Rev. C* **87**, 041304(R) (2013).
- [13] N. Yoshinaga, K. Higashiyama, and P. H. Regan, *Phys. Rev. C* **78**, 044320 (2008).
- [14] G. H. Bhat, W. A. Dar, J. A. Sheikh, and Y. Sun, *Phys. Rev. C* **89**, 014328 (2014).
- [15] T. Nikšić, Z. P. Li, D. Vretenar, L. Próchniak, J. Meng, and P. Ring, *Phys. Rev. C* **79**, 034303 (2009).
- [16] T. Nikšić, D. Vretenar, and P. Ring, *Phys. Rev. C* **78**, 034318 (2008).
- [17] Y. Tian, Z. Y. Ma, and P. Ring, *Phys. Lett. B* **676**, 44 (2009).
- [18] T. Nikšić, D. Vretenar, and P. Ring, *Prog. Part. Nucl. Phys.* **66**, 519 (2011).
- [19] T. Nikšić, P. Ring, D. Vretenar, Y. Tian, and Z. Y. Ma, *Phys. Rev. C* **81**, 054318 (2010).
- [20] Lu Guo, J. A. Maruhn, and P.-G. Reinhard, *Phys. Rev. C* **76**, 034317 (2007).
- [21] D. Vretenar, A. V. Afanasjev, G. A. Lalazissis, and P. Ring, *Phys. Rep.* **409**, 101 (2005).
- [22] J. Meng, H. Toki, S. G. Zhou, S. Q. Zhang, W. H. Long, and L. S. Geng, *Prog. Part. Nucl. Phys.* **57**, 470 (2006).
- [23] P. Ring and P. Schuck, *The Nuclear Many-Body Problem* (Springer-Verlag, Heidelberg, 1980).
- [24] M. Bender, G. F. Bertsch, and P.-H. Heenen, *Phys. Rev. C* **73**, 034322 (2006).
- [25] NNDC National Nuclear Data Center, Brookhaven National Laboratory, <http://www.nndc.bnl.gov>